The characterization of a single discrete bionanodot for memory device applications

2009 Nanotechnology 20 125702

(http://iopscience.iop.org/0957-4484/20/12/125702)

Nanotechnology **20** (2009) 125702 (9pp) doi:10.1088/0957-4484/20/12/125702

The characterization of a single discrete bionanodot for memory device applications

Atsushi Miura[1,2], Ryota Tanaka[1], Yukiharu Uraoka[1,3,5], Nozomu Matsukawa[4], Ichiro Yamashita[1,3,4] and Takashi Fuyuki[1,5]

[1] Graduate School of Materials Science, Nara Institute of Science and Technology, 8916-5 Takayama, Ikoma, Nara 630-0192, Japan
[2] Department of Applied Chemistry and Institute of Molecular Science, National Chiao Tung University, 1001 TaHsueh Road, Hsinchu 30010, Taiwan
[3] CREST, Japan Science and Technology Agency, 4-1-8 Honcho, Kawaguchi 332-0012, Japan
[4] Advanced Technology Research Laboratories, Matsushita Electric Industrial Co., Ltd, 3-4 Hikaridai, Seika, Kyoto 619-0237, Japan

E-mail: uraoka@ms.naist.jp and fuyuki@ms.naist.jp

Received 17 November 2008, in final form 6 February 2009
Published 4 March 2009
Online at stacks.iop.org/Nano/20/125702

Abstract
We investigated electronic properties of a biochemically synthesized cobalt oxide bionanodot (Co-BND) by means of scanning tunneling microscopy/spectroscopy (STM/STS) and Kelvin-probe force microscopy (KFM). Experimentally obtained I–V characteristics and numerically obtained $\mathrm{d}I/\mathrm{d}V$ and $(\mathrm{d}I/\mathrm{d}V)/(I/V)$ from I–V revealed the band gap energy, band position of valence and conduction band of the Co-BND. KFM observation shows that bias polarity dependent surface potential change after charge injection. The observed surface potential change indicates that the Co-BND has a charge storage capability. We demonstrated the application of Co-BNDs for electronic devices by choosing flash memory as the example device. The fabricated Co-BND embedded MOS memory showed clear memory operation due to the charge confinement in the embedded Co-BNDs.

(Some figures in this article are in colour only in the electronic version)

1. Introduction

The usage of biomolecules for the fabrication of nanodevices is a promising direction for nanotechnology. Structural homogeneity based on the same gene information, the inherent capabilities of molecular recognition and the self-assembling nature of biomolecules make them an attractive scaffold for constructing and organizing the functional materials such as the building components of the nanoelectronic devices. Certain types of biomolecules such as viruses, proteins, DNAs and certain amino acid sequences have an ability to recognize and construct inorganic nanomaterials such as nanoparticles [1–5], and nanowires [6–8]. This functionality is called biomineralization. The stringent uniformity of template biomolecules provides structural uniformity of the biomineralized inorganic nanocomposite, and the self-assembling nature of biomolecules enables the ordering of biomineralized nanomaterials to an ordered nanostructure. By taking these advantages, we can fabricate a uniform and well-ordered nanocomponent architecture in the desired small area. Biomolecule mediated inorganic nanomaterial fabrication, organization and its application toward the fabrication of nanoelectronic devices is drawing attention [9–14]. In our approach, we used the genetically engineered cage-shaped supramolecular protein apoferritin to synthesize a uniform nanodot and fabricate its nanoarchitecture. Ferritin is composed from 24 subunits and forms a spherical supramolecular structure with a vacant cavity (figure 1(a) inset). The inner and outer diameters of the protein shell

[5] Address for correspondence: Graduate School of Materials Science, Nara Institute of Science and Technology, 8916-5 Takayama, Ikoma, Nara 630-0192, Japan.

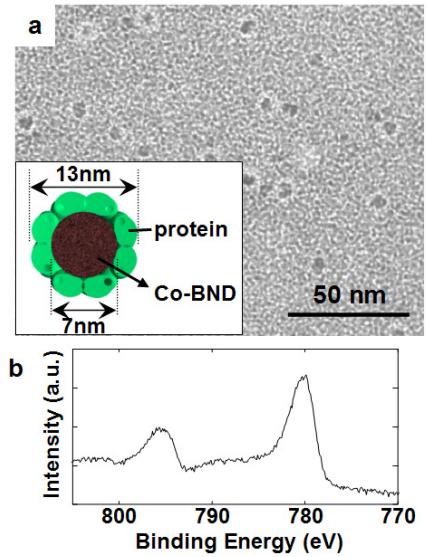

Figure 1. (a) TEM image of the Co-BND in a ferritin protein cage. The protein shell is negatively stained with aurothioglucose. The inset illustrates the schematic cross-sectional drawing of Co-BND accommodated ferritin. (b) XPS spectrum of Co-BND in the Co 2p region.

are about 7 and 13 nm, respectively. It is well known that apoferritin can form many kinds of inorganic nanodot in its protein cage by biomineralization [1–3, 15–17]. We call this biomineralized nanodot a bionanodot (BND). The protein template plays a significant role not only for BND synthesis, but also for controlled, selective and high-density deposition in the nanodot array fabrication on the solid substrate [18–21].

By taking a floating nanodot gate memory (FNGM) as our example device and a biochemically synthesized cobalt oxide (Co_3O_4) bionanodot (Co-BND) and iron oxide bionanodot (Fe-BND) as a charge storage component, we have examined biomolecule utilized solid-state electronic device fabrication and reported the world's first memory operation of BND utilized FNGM [12, 13]. A material diversity of BNDs will offer further improvement of the device properties of BND-FNGM, such as a multi-valued memory device with different BNDs which possess different work functions and/or band gap and single electron transistor applications. However, studies concerning the details of the electronic properties of BND, particularly for a single BND, are limited [22–24]. It is necessary to know the material properties with single molecular resolution for pursuing device fabrication utilizing bioderived nanomaterials.

Scanning probe microscopy (SPM) is a powerful tool, not only for imaging a surface topography, but also for investigating material properties with nanoscale resolution. Scanning tunneling microscopy and spectroscopy (STM/STS) have been used to study the electronic structure of adsorbates such as organic molecule and nanocrystals [25–29]. The tunneling current through the tunnel junction and the differential conductance measured as a function of the bias gives insights for the density of states (DOS) and the band structure of the measured objects. Kelvin-probe force microscopy (KFM) is also a powerful method for investigating the morphological and electronic properties of adsorbates with a nanoscale resolution [30]. KFM is capable of directly and quantitatively imaging the local potential distribution in a thin film. Indeed, AFM based on this method is a useful technique for studying the charge injection to the embedded nanocrystals in an electronic device structure [31–33].

In this contribution, we demonstrate the characterization of the electronic properties of a single cobalt oxide bionanodot, Co-BND, by using STM/STS and KFM. We have used STM/STS to elucidate the electronic band structure of a single Co-BND and KFM to examine the charge storage capability of the single BND by monitoring the potential change after charge injection. We also demonstrate the fabrication and characterization of a Co-BND embedded metal-oxide–semiconductor (MOS) capacitor.

2. Experimental details

2.1. Co-BND synthesis and characterization

Co-BND was synthesized in a recombinant deletion mutant of L-ferritin (Fer8) by one-pot synthesis with ammonium cobalt sulfate as an ion source. Details of expression, overproduction, and purification of apoferritin, and Co-BND synthesis in Fer8 has been described elsewhere [15]. The obtained Co-BND accommodated Fer8 was monitored by transmission electron microscopy (TEM, JEM2200FS, JEOL) to confirm the BND formation in its inner cavity. X-ray photoemission spectroscopy (XPS) was performed to identify the chemical composition of the synthesized Co-BND with monochromatic Al Kα radiation (AXIS165, Kratos). As a reference for the binding energy calibration, the Si 2p peak from Si substrate was used as an internal reference for the calibration. The UV–vis absorption spectra of Co-BNDs were measured on a UV–vis spectrophotometer (UV-1700, Shimadzu). Prior to the ferritin thin film preparation, protein solution was filtered by ultrafiltration with a centrifugal filter device (Ultracel YM-50, Amicon) to displace the 0.05 M Tris-HCl buffer to pure water.

2.2. Single particle characterization by STM/STS and KFM

STM and STS measurements were carried out using an ultra-high-vacuum (UHV) STM system (USM-1200S2J4, Unisoku) to reveal the energy band structure of the synthesized Co-BNDs. All the measurements were done in the UHV chamber of the STM ($<1.0 \times 10^{-8}$ Pa) at room temperature. Mechanically sharpened platinum/iridium (Pt/Ir) wire and highly oriented pyrolytic graphite (HOPG, ZYB grade, GE Advanced Ceramics) was used as a tip and a substrate, respectively. STM images were taken at a sample bias voltage V_s ranging from -2.0 to $+2.0$ V and a constant tunneling current I_t ranging 0.05 to 0.50 nA. During the I–V measurements, the feedback was disabled and data was acquired at constant height. A low concentration aqueous solution of ferritin-Co-BND (0.01 mg ml^{-1}) was used to form 0.6 ML of the ferritin thin film to avoid multilayer formation. The fabricated ferritin-BND architecture was annealed under a N_2 atmosphere at 500 °C to eliminate organic residues such as

protein shell and organic contaminations. We have confirmed that the protein was removed by this annealing treatment [34].

To evaluate the charge storage capability of the single Co-BND, the surface potential change after a bias application was examined by using AFM-based KFM (SPA300HV, Seiko Instruments Inc.). A rhodium-coated conductive silicon (Si) cantilever (SI-DF-3R, Seiko Instruments Inc.) was used. A commercially available Si(100) wafer (p-type, 8.5–11.5 Ω cm) with a 3 nm-thick thermally oxidized silicon dioxide (SiO_2) layer was used as the substrate. A drop (0.1 mg ml^{-1}) of Co-BND accommodated ferritin solution was applied to the SiO_2 surface and rinsed with pure water. The protein shell was removed by UV irradiation under an ozone atmosphere (110 °C, 1 h) [12–14, 19]. Charge injection into and extraction from the Co-BND was carried out by touching a conductive AFM tip to the sample surface in tapping-mode under the applied substrate bias voltage [31, 33]. Following the charging to and discharging from the Co-BNDs, the topographic and surface potential images were simultaneously obtained with a non-contact KFM scan. All KFM measurements were performed at room temperature.

2.3. Device fabrication and characterization

The Co-BND FNGM devices were fabricated to examine the application of Co-BNDs as the charge storage node of flash memory. Details of the device fabrication process is described elsewhere [12, 14]. Briefly, Co-BND ferritin deposition on the Si substrate and protein elimination was carried out with the same procedure as done for the KFM sample preparation. The fabricated Co-BND array was buried in a control gate SiO_2. The areal density of the embedded Co-BNDs was obtained as 6.4×10^{11} cm^{-2} from scanning electron microscopy observations. The aluminum gate electrode deposition and post metal annealing under a N_2 atmosphere at 300 °C finalized the MOS capacitor fabrication. The electrical characterization of the fabricated Co-BND embedded MOS capacitors was performed by capacitance–voltage (C–V) measurements with an HP 4284A LCR meter.

3. Results and discussions

3.1. Synthesis and characterization of Co-BND in protein cage

Figure 1(a) shows a TEM image of synthesized Co-BND in the ferritin protein cage. A schematic cross-sectional drawing of the protein cage of ferritin and accommodated Co-BND is depicted in the inset. The synthesized BNDs appear as spherical black dots surrounded by a negatively stained protein envelope which appears white in the TEM image. From the analysis of the TEM images, the BND formation ratio and average diameter are estimated to be more than 95% and 6.6 ± 0.5 nm, respectively [14, 15]. Figure 1(b) shows the XPS spectrum obtained with the fabricated Co-BND. The main peaks at 780.2 and 795.7 eV and weak satellite structures at 788.8 and 804.2 eV in the XPS spectrum are clear evidence of the chemical composition of the BND as Co_3O_4. These peaks are assigned to the signals from Co $2p_{3/2}$ and $2p_{1/2}$ of Co_3O_4, respectively. The spectrum obtained agrees well with that of Co_3O_4 reported [35].

3.2. Electronic property of single Co-BND by STM/STS

The Co-BNDs deposited on the HOPG after protein elimination were viewed by STM with $I_t = 0.15$ nA and $V_s = +1.7$ V (figure 2(a)). The STM image observed shows a loosely packed arrangement of deposited Co-BNDs. The center-to-center distance between neighboring BNDs is larger than the 13 nm which corresponds to the outer diameter of ferritin protein. Therefore the Co-BNDs are not connected. This result indicates that the protein shell of ferritin precludes direct contact of neighboring Co-BNDs. Individual BNDs are isolated and identified for I–V measurements. The observed BNDs showed well defined particle sizes of about 7 nm. This value corresponds well to the inner cavity size of the ferritin molecule and the average diameter obtained from TEM analyses. The deposited Co-BNDs are frequently found predominantly at the step edge of the HOPG substrate.

To investigate the electronic band structure, single molecule I–V measurements were examined on top of the Co-BND observed in figure 2(a). Figure 2(b) shows a representative I–V curve measured on top of the Co-BND. For comparison, a spectrum taken on the HOPG is also depicted (dashed line in figure 2(b)). The I–V curve obtained for the HOPG shows the typical I–V characteristics of a metallic conductor. The spectrum shows a continuous change of the tunneling current with no zero conductance region. In contrast to the HOPG, the I–V curve of the Co-BND (solid line) shows a suppressed tunneling current around zero bias voltage and an increasing current flow from the edge of this region. The observed increase of current flow is considered as due to the interaction of the DOS of the metal tip and the Co-BND. Therefore, the edges and the width of zero conductance region is correlated with the resonant tunneling through occupied states (i.e. valence band at negative bias), unoccupied states (i.e. conduction band at positive bias) of the Co-BND and the band gap of Co-BND, respectively. The almost symmetric spectral shape of the I–V curves obtained indicate that holes and electrons almost equally contribute to the charge transport in the unoccupied and occupied state. The tunneling spectra of nanoparticle strongly depends on tunneling parameters such as gap distance and tunneling configuration, and it makes the determined band gap unreliable [25]. Meanwhile, the I–V characteristics of Co-BNDs obtained by varying the set point and substrate bias showed quite similar band gap widths. Therefore, we can conclude that the distance between tip and sample is sufficiently large for the detection of non-perturbed spectra.

The tunneling conductance dI/dV is considered to reflect the DOS of the measured material. The gap edge defined by the intersection of the tangent of the platform and the uplifted part of the dI/dV spectrum is considered to represent the edge of the valence and conduction band. Determined from the calculated dI/dV spectra (not shown), the band gap of the Co-BNDs are roughly estimated to be ∼2 eV. To visualize the band gap, as well as the positions of valence and conduction band, more clearly, we calculated the normalized tunneling conductance $(dI/dV)/(I/V)$ from I–V and dI/dV data using a simple offset method [36]. The $(dI/dV)/(I/V)$ versus V (figure 2(c)) clearly show the band gap and the positions of

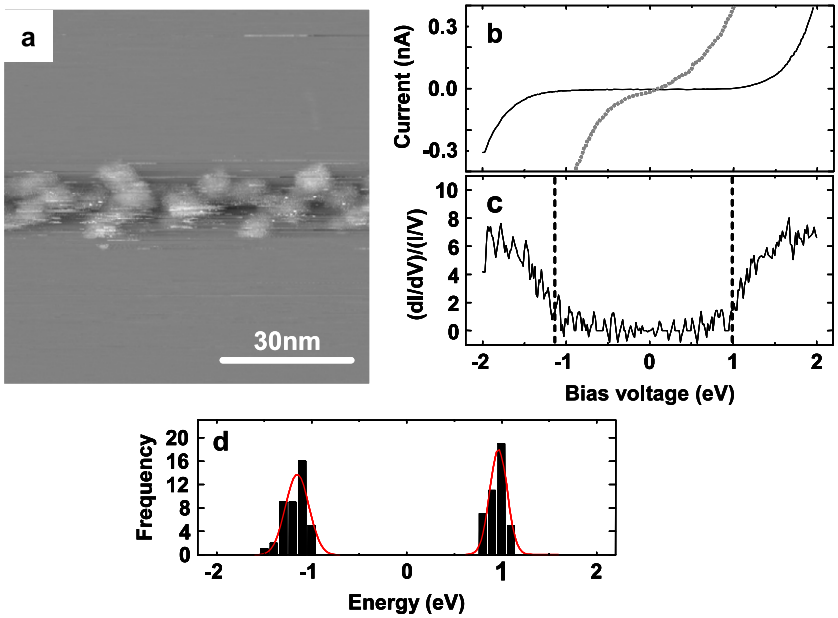

Figure 2. (a) STM image of the Co-BND on the HOPG. $I_t = 0.15$ nA, $V_s = +1.7$ V. (b) I–V curves measured on top of the Co-BND (solid line) and the HOPG (dotted line). (c) Normalized tunneling conductance $(\mathrm{d}I/\mathrm{d}V)/(I/V)$ numerically obtained from I–V depicted in (b). (d) Histogram of the valence and conduction band position. Vertical dashed lines depicted in (c) represent the positions of the average valence and conduction band, -1.1 and $+1.0$ eV, respectively.

valence (E_V) and conduction (E_C) bands. The sharp increase at around -1 and $+1$ V corresponds to the valence and the conduction band edges, respectively. The histogram shown in figure 2(d) is constructed from the values of E_V and E_C obtained from 44 sample data to present the distribution of band position. From figure 2(d), the position of E_V and E_C is 1.1 ± 0.2 eV below and 1.0 ± 0.1 eV above with respect to the Fermi level of the HOPG (4.7 eV), [29] and the band gap is obtained as 2.1 ± 0.2 eV.

The band gap width of ∼2.1 eV obtained is consistent with the energy gap which is the optically observed direct transition between the valence and conduction bands of cobalt oxide (Co_3O_4, 1.8–2.2 eV) [37–40]. The UV–vis absorption spectrum of Co-BND deposited on glass substrate is shown in figure 3(a). We should note that the protein shell of ferritin was thoroughly removed. Therefore, the absorption spectrum represents the optical characteristics of the Co-BND. As has been investigated in the literature, in Co_3O_4, the valence band has a strong O 2p character, while the main contribution to the conduction band is given by the Co (II) 3d orbital [39]. The absorption observed around 600–700 nm is correlated to the direct transition from the O 2p to Co (II) 3d orbital. Figure 3(b) shows the Tauc plot $(\alpha h\nu)^2$ of the Co-BND film obtained from figure 3(a). It is well-established that the dependence of the absorption coefficient, α, is given by the following classical expression,

$$\alpha(h\nu) = A(h\nu - E_g)^n, \tag{1}$$

where $h\nu$, E_g, and A represents the photon energy, the optical band gap, and a constant [37, 38]. The exponent n takes different values depending upon the types of electronic transition in the k-space. Assuming a direct transition with n equal to $1/2$, the plots of $(\alpha h\nu)^2$ versus $h\nu$ are yielded. The

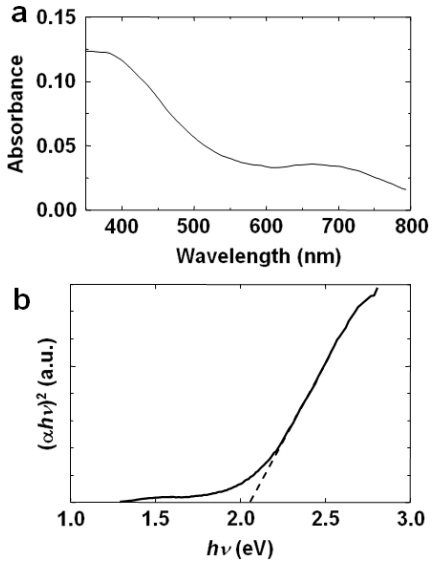

Figure 3. (a) Absorption spectrum of the Co-BND on a glass substrate after protein elimination and (b) Tauc plot $(\alpha h\nu)^2$ of the observed absorption spectrum with $n = 1/2$ as a function of photon energy.

optical band gap energy can be obtained by extrapolating the $h\nu$ to $\alpha = 0$. We can determine the band gap energy of Co-BND as 2.05 eV from figure 3(b). The optical band gap energy obtained, 2.05 eV, due to the direct transition from the valence band to the conduction band, is consistent with the band gap obtained from STS measurements. Therefore, we can conclude that we could directly observe the band gap energy of Co-BND by means of STS measurements.

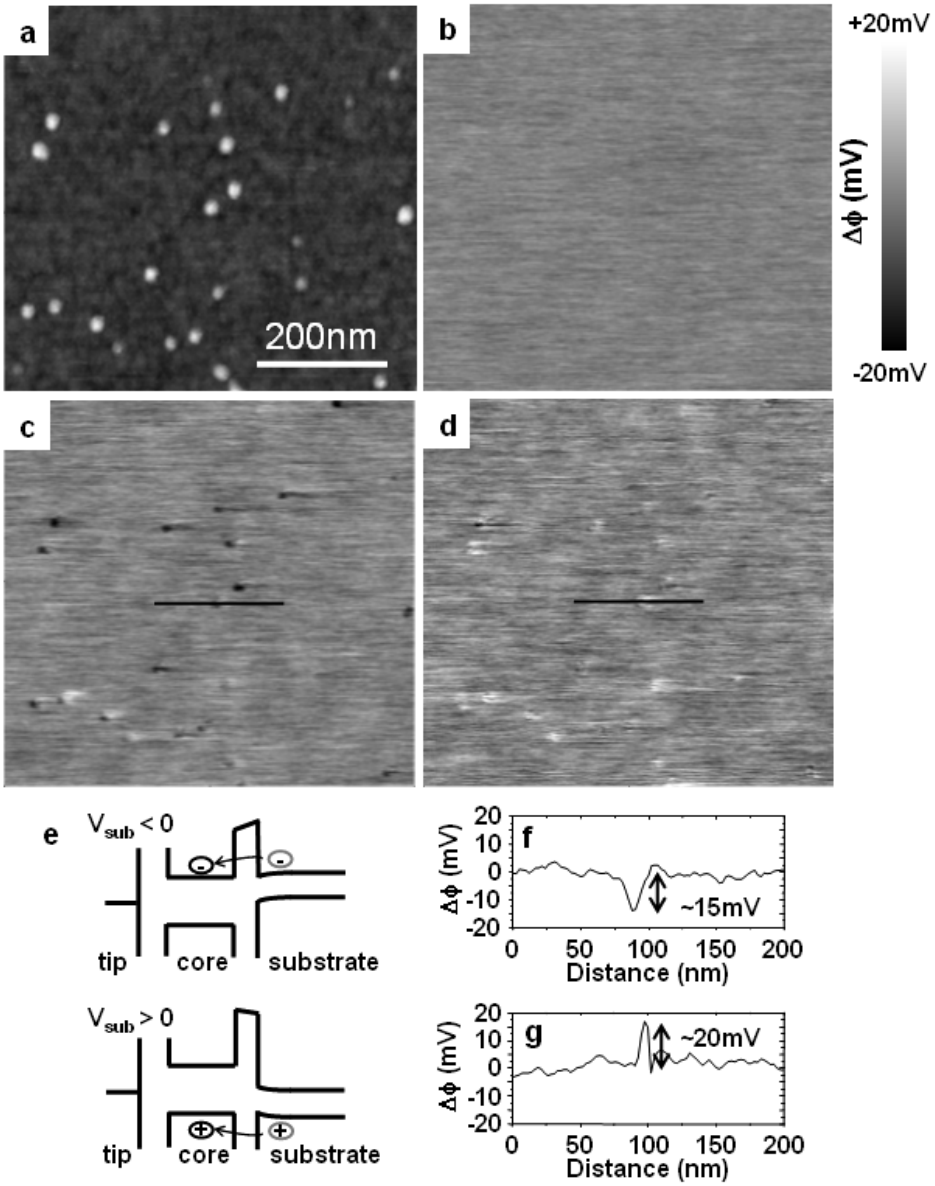

Figure 4. (a) Topographic and (b)–(d) corresponding potential images obtained by KFM. Potential images were measured (b) before applying the substrate bias and after applying (c) −2 V and (d) +2 V to the substrate, respectively. (e) Schematic energy band diagram explaining the electron injection at a negative substrate bias and hole injection at a positive substrate bias; (f) and (g) show the cross-sectional potential profile along the line indicated in (c) and (d), respectively.

3.3. Charge storage capability of Co-BND

We used KFM observation to evaluate the charge storage capability of the single Co-BND. A topographic and corresponding potential images of Co-BNDs deposited on a Si wafer are depicted in figures 4. It should be noted that the outer protein shell is removed by oxidation prior to the KFM measurements. The average height of the Co-BNDs, which are sparsely distributed in the topographic image (figure 4(a)), is determined as 6.4 ± 0.2 nm from the cross-sectional analysis of the topography. The potential images presented in figures 4(b)–(d) were observed before applying the substrate bias, and after applying −2 V and +2 V to the substrate, respectively. In the potential images, bright corresponds to a higher and dark corresponds to a lower potential with respect to the substrate surface. In figure 4(b), we observed no surface potential difference between the deposited Co-BNDs and the surrounding SiO_2 surface in which bias voltage was not applied. On the other hand, after applying −2 V (figure 4(c)) and +2 V (figure 4(d)), we observed a surface potential change at the point where the Co-BNDs were observed in the topography. From time duration experiments, we observed that this potential change can be retained for at least 120 min. The Co-BNDs in figures 4(c) and (d) appeared darker and brighter relative to the surrounding Si substrate surface, respectively. The observed negative and positive potential change indicates negative and positive charge injection to the BNDs, more specifically, electron and hole injection to the Co-BND depending upon the applied bias polarity. The observed potential change

is a clear indication of the charge storage capability of Co-BND.

The potential changes observed under bias application are consistently explained by using the schematic energy band diagrams depicted in figure 4(e). When the negative bias voltage was applied to the substrate, the energy level of the Si substrate became high and an electron was injected into the Co-BND from the Si substrate. As a result, the surface potential of the Co-BNDs became lower and appeared darker in the potential image. In contrast, hole injection to the Co-BND was carried out when the energy level of the substrate became lower by applying the positive bias voltage to the substrate. Consequently, the surface potential of the Co-BNDs became higher compared to the surrounding Si substrate surface. An applied bias polarity dependent electron and hole injection behavior is similarly observed in the device property measurements of Co-BND embedded MOS capacitors and MOS transistors [12, 14, 18]. Therefore, the charge injection mechanism for MOS devices and for KFM observation is analogous. From the observed charge injection behavior, the relative positions of the valence and conduction bands are considered to be positioned above and below the conduction and valence bands of the Si substrate, respectively.

Figures 4(f) and (g) represent the surface potential cross-section of Co-BND after a −2 and +2 V bias application, respectively. The surface potential cross-section was measured along the line indicated in figures 4(c) and (d). The cross-section of surface potential quantitatively gives the potential change after charge injection. The bias application induced about 15–20 mV of potential decrease (figure 4(f), −2 V) and increase (figure 4(g), +2 V) of the Co-BND in comparison to that of surrounding SiO_2 surface. We can estimate the number of electrons injected into the BND by comparing the measured potential change with the calculated charging energy of the BND from the following equations [41, 42].

$$W = (n^2 e)/C_{\mathrm{BND}}, \tag{2}$$

where W is the charging energy, n is the number of injected charges and e is the magnitude of the elementary charge. The self-capacitance of the BND, C_{BND}, is represented as $C_{\mathrm{BND}} = 4\pi\varepsilon r$ by assuming the BND as a conductive sphere, where r is the radius of the Co-BND (3.2 nm) and ε is its dielectric constant. The dielectric constant of Co_3O_4 is unknown. Therefore, we assumed $\varepsilon = 12.9$, which is the dielectric constant of CoO. [38] Following this calculation, charging energies of ∼18 and ∼70 meV are obtained for one and two electrons retained in a single BND, respectively. The experimentally obtained potential change is close to the forecasted value for single electron storage in a single BND.

We should note that the calculated value of the single electron charging energy, ∼18 meV, is smaller than the thermal energy and it is very difficult to observe such a small energy change at room temperature. In reality, we observed the potential change on most of the BNDs, but we did not observe the potential change on some BNDs. On these BNDs, the injected charges may be withdrawn due to fluctuations of thermal energy. Even though the observation of such small energy change was very difficult at room temperature, we could confirm the reproducibility of the potential change experimentally. Therefore, the potential change observed in the KFM images is attributed to the reflection of a stored single charge.

The observed single charge storage behavior is ascribed to the energy band structure of Co-BND. Figure 5 depicts the topographic, potential images and corresponding surface potential cross-section curves at the point where the potential change was observed. Charge injection was carried out by applying −5 and +5 V, in figures 5(b) and 5(c), respectively. Figures 5(d) and 5(e) depict the surface potential cross-section curves which were measured in figures 5(b) and 5(c), respectively. BNDs on the line, which is indicated in figures 5(b) and (c) showed negative and positive potential changes of 25–30 mV, respectively. As we mentioned above, the BND will show ∼70 mV of potential change if two charges are stored in the single BND. However, the observed potential changes, ∼25 mV for electron charging by −5 V and ∼27 mV for hole charging by +5 V, were similar to the values observed in figures 4(f) and (g). The observed potential changes are too small to assign as multicharge storage to the single BND. We have examined the applied bias voltage dependence of the potential change from −5 to +5 V. However, the observed potential change ranged between 20–30 mV, and we could not observe any significant applied bias dependence. These results indicate that an increase of charging voltage did not induce an increase of potential change. In other word, we could increase the number of 'injected' charges, but the number of 'stored' charges could not increased by strengthening the applied electrical field.

In the case of Co-BND embedded MOS devices, we could increase the number of 'stored' charges by increasing the number of 'injected' charges with strengthening of the applied electrical field. In that case, embedded the cobalt oxide Co-BND is converted to a hybrid of metal cobalt and cobalt oxide due to the post annealing process after device fabrication. A deep potential well is formed between metal cobalt and cobalt oxide and worked efficiently for charge storage in the case of MOS devices [14]. Meanwhile, in the present case, Co-BND exists as cobalt oxide, and the valence and conduction bands of Co-BND are positioned below and above those of Si, respectively. Thus electrons injected to the conduction band and holes injected to the valence band easily tunneled back to Si when the substrate bias voltage was turned off, i.e. at the flat band condition where potential imaging was carried out. Even if we apply a stronger electric field in order to 'inject' a lot of electrons and holes into the Co-BND, the injected charges will spontaneously tunnel back to the Si substrate due to the higher band energy with respect to that of the Si substrate. Therefore we could not increase the number of 'stored' charges by applying a higher electrical field in this case. From these results, the observed potential change does not reflect the number of 'injected' charges to the single BNDs but the 'stored' charge after charge injection. The KFM results obtained indicate that the cobalt oxide Co-BND has a relatively poor charge storage ability in conjunction with Si. However, the observed very small potential change and the endurance of stored charge for two hours still indicate a charge

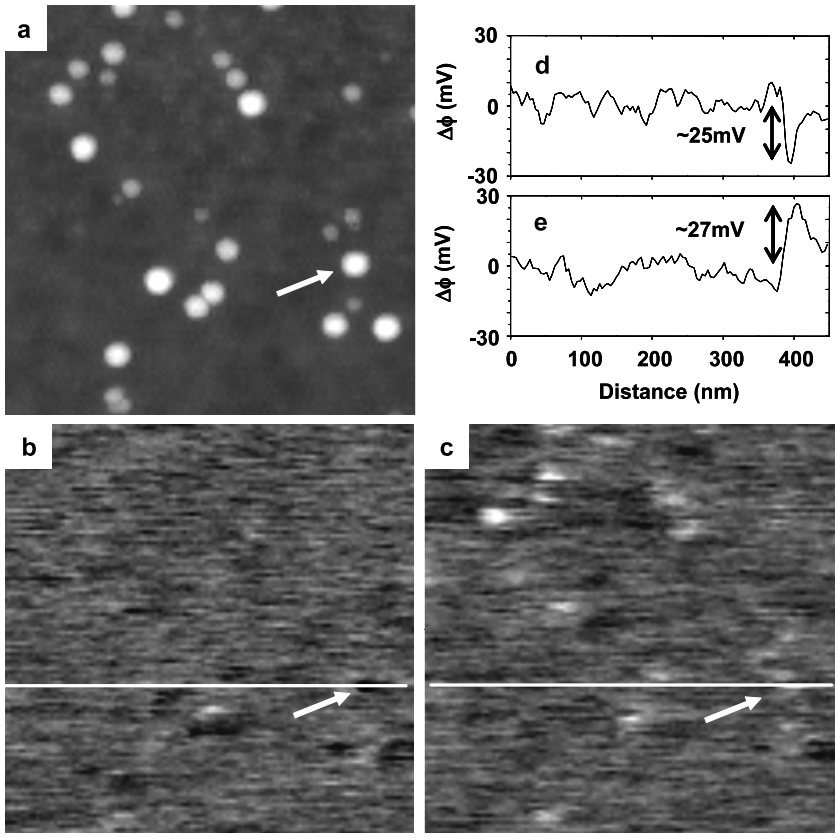

Figure 5. (a) Topographic image and potential images obtained by KFM after applying (b) −5 V and (c) +5 V, respectively. Cross-sectional profile of the potential change after applying (d) −5 V and (e) +5 V measured along the line indicated in (b) and (c). Arrows in potential images indicate the position of the corresponding BND in the topographic image.

storage ability in the Co-BND. We should find other pairings of different wide band gap materials for the utilization of as-prepared cobalt oxide Co-BND.

3.4. Memory characteristics of Co-BND embedded MOS device

Keeping in mind that the cobalt oxide Co-BND has a relatively poor charge storage ability, we examined the Co-BND application as the charge storage node of an FNGM by fabrication of a Co-BND embedded MOS capacitor. The high-frequency C–V characteristics of the Co-BND embedded MOS capacitor are shown in figure 6(a). We should note that the embedded Co-BNDs remained as cobalt oxide Co_3O_4 even after the annealing process, because the annealing was carried out in a nitrogen atmosphere at 300 °C. The XPS spectrum of the annealed Co-BND which was embedded in a SiO_2 gate stack (figure 6(b)) showed main peaks at 780.2 and 795.7 eV like the as-prepared Co-BND depicted in figure 1(b). Therefore, it is confirmed that embedded Co-BNDs in the MOS capacitor structure exist as cobalt oxide Co_3O_4. In the C–V measurement, the gate voltage was swept from −8 V (accumulation) to +6 V (inversion) and then back to −8 V. Under the gate voltage scan, we observed an anti-clockwise hysteresis in the C–V characteristics as shown in figure 6(a). In stark contrast, the MOS capacitor without any Co-BND showed neither a lateral shift nor an anti-clockwise hysteresis (data not shown). As we previously reported, the observed anti-clockwise hysteresis is obvious evidence of a charge confinement to the embedded Co-BNDs [12, 14]. Therefore, the observed anti-clockwise hysteresis in the C–V characteristics indicates that a non-reduced Co-BND possesses an ability to store a charge. The typically observed memory window width, 0.4–0.5 V, was much smaller than a previously reported value of more than 2.6 V [14]. Based on the number of embedded Co-BNDs (6.4×10^{11} cm^{-2}), which was confirmed by scanning electron microscopy, and a memory window width of 0.4 V observed in figure 6(a), the number of stored charges in the single BND is estimated to be 0.7 from the following equation, [14]

$$\Delta V_{FB} = [ned_{\mathrm{dot}}(t_{\mathrm{gate}} + \tfrac{1}{2}D_{\mathrm{dot}})]/\varepsilon_{\mathrm{OX}}. \quad (3)$$

Here, n, d_{dot}, t_{gate}, D_{dot} and ε_{ox} are the charge number per single Co-BND, the aerial density of Co-BNDs, the thickness of the control gate oxide (20 nm), the diameter of the Co-BND (6.6 nm) and the dielectric constant of SiO_2, respectively. Even though the applied electrical field for charge injection was sufficiently strong, the number of stored charges in the embedded Co-BNDs was quite small. It is consistent with the single charge retention observed in the KFM potential image. The potential images obtained in all electric field strengths showed similar potential changes of 15–30 mV, although the injected charge numbers should become larger depending on

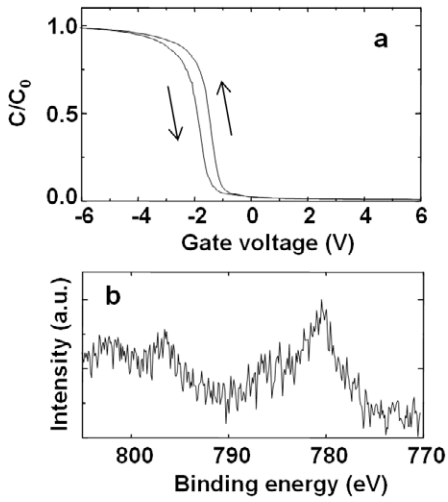

Figure 6. (a) High-frequency capacitance–voltage characteristics of a Co-BND embedded MOS capacitor. (b) XPS spectrum of Co-BND stacked in a SiO_2 thin film.

the applied field strength. As we mentioned in the previous section, when the cobalt oxide Co-BND is used with Si, it has poor charge storage capability due to its band energy position with respect to that of Si substrate. The small memory window width observed, i.e. very small number of stored charges, is due to the leakage of injected charges from the BNDs. Although the cobalt oxide Co-BND has a poor charge storage ability, the anti-clockwise hysteresis in the C–V characteristics clearly indicates that a Co-BND can confine charges, and its charge storage ability is important for band energy utilized charge programming to the embedded charge storage node of a nanodot memory.

4. Conclusions

In conclusion, we have examined the electronic characteristics of a biochemically synthesized cobalt oxide Co-BND in a supramolecular protein cage with single molecule resolution. From the STM/STS measurements we have revealed the band gap energy of biomineralized Co-BND as 2.1 eV. The relative positions of the valence and conduction bands is also estimated to be 1.1 eV below, and 1.0 eV above, the Fermi level of HOPG from the numerical analysis of spectral data. From the KFM measurements, we confirmed the charge storage capability of a single Co-BND by observing the surface potential change of the single Co-BND after charge injection. The surface potential of the BNDs changed depending upon the polarity of applied bias. These results indicated that electron and hole injection was carried out depending on the polarity of applied substrate bias. In addition, the relative band position of the Co-BND and Si substrate was estimated. The conduction and valence band of Co-BNDs lie above and below those of the Si substrate. We also observed the applied electric field strength independent potential change of single BNDs. This suggests that the charge storage capability of the Co-BND is relatively small in combination with Si. We need to be more careful with the choice of substrate material, such as other kinds of wide band gap materials, for effective charge storage applications of the Co-BND. The C–V characteristics of the cobalt oxide Co-BND embedded MOS capacitor indicate that the as-prepared Co_3O_4 Co-BND possess an ability to store charge without a reduction to the metal Co. These results indicate that SPM characterization is a powerful method to probe the electronic properties of inorganic nanoparticles, which are potential materials for nanoelectronic device fabrication, with single molecule resolution.

Acknowledgments

The authors would like to acknowledge Dr M Okuda and K Nishio at Panasonic for the overproduction and purification of recombinant ferritin used in this study. This work was supported by a Leading Project of the Ministry of Education, Cultures, Sports, Science and Technology (MEXT), Japan.

References

[1] Dougras T and Young M 1998 *Nature* **393** 152
[2] Yamashita I 2006 *IEDM Tech. Dig.* vol 447
[3] Meldrum F C, Wade V J, Nimmo D L, Heywood B R and Mann S 1991 *Nature* **349** 684
[4] Kramer R M, Li C, Carter D C, Stone M O and Naik R R 2004 *J. Am. Chem. Soc.* **126** 13282
[5] Lee S W, Mao C, Flynn C E and Belcher A M 2002 *Science* **296** 892
[6] Mao C, Solis D J, Reiss B D, Kottmann S T, Sweeney R Y, Hayhurst A, Georgiou G, Iverson B and Belcher A M 2004 *Science* **303** 213
[7] Tsukamoto R, Iwahori K, Muraoka M and Yamashita I 2005 *Bull. Chem. Soc. J.* **78** 2075
[8] Bai H Y, Xu K, Xu Y J and Matsui H 2007 *Angew. Chem. Int. Edn* **46** 3319
[9] Shan T, Chuanbin M, Yueran L, Kelly D Q and Banerjee S K 2005 *IEDM Tech. Dig.* vol 174
[10] Nam K T, Kim D-W, Yoo P J, Chiang D C-Y, Meethong N, Hammond P T, Chiang D Y-M and Belcher A M 2006 *Science* **312** 885
[11] Tseng R J, Tsai C, Ma L, Ouyang J, Ozkan C S and Yang Y 2006 *Nat. Nanotechnol.* **1** 72
[12] Miura A, Hikono T, Matsumura T, Yano H, Hatayama T, Uraoka Y, Fuyuki T, Yoshii S and Yamashita I 2006 *Japan. J. Appl. Phys.* **45** L1
[13] Hikono T, Matsumura T, Miura A, Uraoka Y, Fuyuki T, Takeguchi M, Yoshii S and Yamashita I 2006 *Appl. Phys. Lett.* **88** 023108
[14] Miura A, Uraoka Y, Fuyuki T, Yoshii S and Yamashita I 2008 *J. Appl. Phys.* **103** 074503
[15] Tsukamoto R, Iwahori K, Muraoka M and Yamashita I 2005 *Bull. Chem. Soc. J.* **78** 2075
[16] Iwahori K, Yoshizawa K, Muraoka M and Yamashita I 2005 *Inorg. Chem.* **44** 6393
[17] Okuda M, Iwahori K, Yamashita I and Yoshimura H 2003 *Biotechnol. Bioeng.* **84** 187
[18] Miura A, Uraoka Y, Fuyuki T, Kumagai S, Yoshii S, Matsukawa N and Yamashita I 2007 *Surf. Sci.* **601** L81
[19] Yamada K, Yoshii S, Kumagai S, Miura A, Uraoka Y, Fuyuki T and Yamashita I 2006 *Japan. J. Appl. Phys.* **45** 8946
[20] Matsui T, Matsukawa N, Iwahori K, Sano K I, Shiba K and Yamashita I 2007 *Langmuir* **23** 1615
[21] Kumagai S, Yoshii S, Yamada K, Matsukawa N, Fujiwara T, Iwahori K and Yamashita I 2006 *Appl. Phys. Lett.* **88** 153103

[22] Preisinger M, Krispin M, Rudolf T, Horn S and Strongin D R 2005 *Phys. Rev.* B **71** 165409
[23] Liu G, Debnath S, Paul K W, Han W Q, Hausner D B, Hosein H A, Michel F M, Parise J B, Sparks D L and Strongin D R 2006 *Langmuir* **22** 9313
[24] Xu D G, Watt G D, Harb J N and Davis R C 2005 *Nano Lett.* **5** 571
[25] Bakkers E P A M and Vanmaekelbergh D 2000 *Phys. Rev.* B **62** 7743
[26] Deng W and Hipps K W 2003 *J. Phys. Chem.* B **107** 10736
[27] Nazin G V, Qiu X H and Ho W 2003 *Science* **302** 77
[28] Uji-i H, Miura A, Schenning A, Meijer E W, Chen Z J, Wurthner F, De Schryver F C, Van der Auweraer M and De Feyter S 2005 *ChemPhysChem* **6** 2389
[29] Miura A, Chen Z J, Uji-i H, De Feyter S, Zdanowska M, Jonkheijm P, Schenning A P H J, Meijer E W, Wurthner F and De Schryver F C 2003 *J. Am. Chem. Soc.* **125** 14969
[30] Stern J E, Terris B D, Mamin H J and Rugar D 1988 *Appl. Phys. Lett.* **53** 2717
[31] Nishitani J, Makihara K, Ikeda M, Murakami H, Higashi S and Miyazaki S 2006 *Thin Solid Films* **508** 190
[32] Salem M A, Mizuta H and Oda S 2004 *Appl. Phys. Lett.* **85** 3262
[33] Kubota T, Hashimoto T, Ishikawa Y, Samukawa S, Miura A, Uraoka Y, Fuyuki T, Takeguchi M, Nishioka K and Yamashita I 2006 *Appl. Phys. Lett.* **89** 233127
[34] Yoshii S, Yamada K, Matsuskawa N and Yamashita I 2005 *Japan. J. Appl. Phys.* **44** 1518
[35] Schumacher L C, Holzhueter I B, Hill I R and Dignam M J 1990 *Electrochim. Acta* **35** 975
[36] Prietsch M, Samsavar A and Ludeke R 1991 *Phys. Rev.* B **43** 11850
[37] Patil P S, Kadam L D and Lokhande C D 1996 *Thin Solid Films* **272** 29
[38] Cheng C S, Serizawa M, Sakata H and Hirayama T 1998 *Mater. Chem. Phys.* **53** 225
[39] Barreca D, Massignan C, Daolio S, Fabrizio M, Armelao L and Tondello E 2001 *Chem. Mater.* **13** 588
[40] Gulino A, Dapporto P, Rossi P and Fragala I 2003 *Chem. Mater.* **15** 3748
[41] Lee C, Meteer J, Narayanan V and Kan E C 2005 *J. Electron. Mater.* **34** 1
[42] Yang G, Tan L, Yang Y, Chen S and Liu G Y 2005 *Surf. Sci.* **589** 129